Published online June 30, 2017

Pore-Size Distributions of Soils Derived using a Geometrical Approach and Multiple Resolution MicroCT Images

Fabio Augusto Meira Cássaro*
State Univ. of Ponta Grossa
Dep. of Physics
Ponta Grossa
PR, 84030-900
Brazil

Adolfo Nicolas Posadas Durand
International Potato Center
P.O. Box 1558
Lima
Peru

Daniel Gimenez
Rutgers University
Dep. of Environmental Science
New Brunswick, NJ 08901

Carlos Manoel Pedro Vaz
Embrapa Instrumentação
P.O. Box 741
São Carlos
SP, 13560-970
Brazil

Soil pores form interconnected networks that directly or indirectly influence transport processes in soils. There is great interest in estimating pore properties such as size and shape from three-dimensional (3D) images as a way of understanding linkages between structure and function. This work evaluates the applicability of an approach to measure pore-size distributions (PSDs) from 3D images of four soils with contrasting physical properties. Images were obtained with a benchtop X-ray microtomograph system at spatial resolutions of 4, 6, 12, and 30 μm by varying the size of the samples from 0.5 cm to about 4 cm in diameter. Pore-size distributions obtained at each image resolution were fitted with lognormal distribution functions with r^2 ranging from 0.81 to 0.98. The four PSDs for a given soil were combined by identifying crossover points in the lognormal distributions. When pore sizes where imaged at more than one resolution, the criterion followed to eliminate redundant information was that large pore sizes are better represented in low resolution images of large sample sizes, and vice versa. Pore-size data from four truncated PSDs were fitted with a lognormal distribution function to obtain a final (global) PSD for each soil. Global PSDs obtained with the image-based approach correlated well with PSDs measured by mercury intrusion porosimetry and also with PSDs derived from soil water retention curves, showing potential for application of this image-based approach to soils.

Abbreviations: CT, computed tomography; microCT, microtomography; MIP, mercury intrusion porosimetry; PSD, pore-size distributions; SWRC, woil water retention curve; VOI, volume of interest; 3D, three dimensional.

Core Ideas

- **X-ray microtomography.**
- **An image-based approach to determine soil pore distributions.**
- **Integration between information obtained in different spatial resolutions.**

Soil pore networks are complex interconnected lattices responsible for conducting water, air, and solutes, and for sustaining roots and the microbiota. Pore-size distributions are particularly suitable for evaluating natural (pedogenetic) or anthropogenic induced changes in soil structure (Jassogne et al., 2007; Taina et al., 2010; Dal Ferro et al., 2012). Estimates of PSD are commonly derived from standard water-desorption measurements that generate soil water retention curves (SWRC; Mishra and Sharma, 1988; Cássaro et al., 2011) or by mercury intrusion porosimetry (MIP; Zhang and Li, 2010). On the other hand, imaging techniques such as X-ray computed tomography (CT) or photographs of resin-impregnated soil sections allow direct examination of soil pore structure and quantification of pore area, volume, size, and shape characteristics and their spatial location in the soil pore system (Vogel and Roth, 1998; Cnudde and Boone, 2013). Recent advances in X-ray microtomography (microCT) have facilitated acquiring high resolution 3D images of soils and rocks and has opened the possibility of extending studies on the geometry of natural porous media to small pores (Helliwell et al., 2013; Wildenschild and Sheppard, 2013; Peth et al., 2008; Vaz et al., 2011).

Estimation of PSDs from water retention data assumes pore systems as bundles of cylindrical tubes and applies the capillary rise equation to determine

Soil Sci. Soc. Am. J. 81:468–476
doi:10.2136/sssaj2016.09.0291
Received 19 Sep. 2016.
Accepted 3 Mar. 2017.
*Corresponding author (fcassaro@uepg.br).

equivalent pore radii, whereas in the MIP method the Washburn equation is used to relate the applied pressures to equivalent pore radii (Flint and Flint, 2002). Estimation of water retention properties from 3D images also uses the capillary model to convert pore radii to pressure potentials (Rab et al., 2014; Dal Ferro et al., 2015). The capillary model is of straightforward application but it may fail to predict the experimental data because it does not consider connection among the cylindrical pores (Vogel and Roth, 1998; Hunt et al., 2013). In contrast, pore-network models are difficult to implement but can provide a more realistic estimation of SWRCs because they account for geometrical parameters such as pore coordination number, pore-(nodal) and throat-size distributions (Vogel and Roth, 1998).

A relatively simple algorithm for determining PSD from images was proposed by Yang et al. (2009), in which disks (2-D case) or spheres (3-D case) are iteratively fitted into digitized pore units, varying from a largest identified radius to a minimum radius (pixel or voxel size). Each step is associated with an incremental area or volume and the PSD is estimated by relating the invaded area or volume to its critical radius, scaled by pixel size (Fig. 1). In Fig. 1, the intruded area or volume is determined by removing pixels belonging to Region A_1 (critical radius r_1), from Region A_i (critical radius r_i). In Fig. 1c and 1d, A_{i-1} represents the difference in area between these last two steps. This process is geometrically analogous to the steps taken during the mercury intrusion technique, in which pressure is increased in steps to force mercury into progressively smaller pores, that is, A_{i-1} represents the area or volume that is intruded as the applied external pressure is increased from $P_1 = P(r_1)$ to $P_i = P(r_i)$, with $r_i < r_1$. The procedure of fitting objects of incrementally smaller radii accounts for the entire discretized pore space while avoiding any volume overlapping. Although this procedure does not provide geometrical parameters of the pore system, it seems very promising for quantifying PSD of soils or other related porous media due to its similarity to a fluid filling approach, providing a more realistic PSD in terms of water retention functionalities.

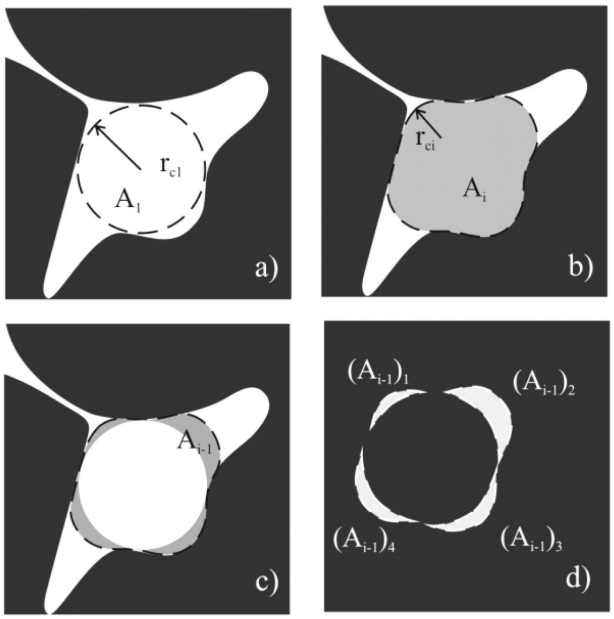

Figure 1. Sketch showing the pore intrusion approach of Yang et al. (2009): (a) First critical radius r_{c1}; (b) *i*th iteration showing the *i*th-critical radius; (c) Incremental area between the first and the *i*th step; (d) Incremental area divided in a set of four components.

A limitation of microCT images for representing PSDs is that there is a tradeoff between sample size and image spatial resolution (Vaz et al., 2011; Rab et al., 2014) that could prevent a complete representation of a pore system when only one sample size/image resolution is used. Therefore, image resolution is typically determined by the objective of the research; macro and meso porosity are usually studied with images having voxel sizes (resolutions) varying from 20 μm to several hundred microns (Pierret et al., 2002; Jassogne et al., 2007; Dal Ferro et al., 2015), whereas intra-aggregate porosity is characterized with resolutions ranging between approximately 3 and 15 μm (Peth et al., 2008; Wang et al., 2012; Ma et al., 2015). Imaging pore systems at more than one resolution has been done for methodological purposes (Císlerová and Votrubová, 2002; Rab et al., 2014) or for better characterization of the porosity (Papadopoulos et al., 2009; Dal Ferro et al., 2013), but in rare cases more than two resolutions are used (e.g., Rab et al., 2014).

A more complete characterization of PSDs from images would require estimating pore sizes from images taken at multiple resolutions and combining the information from each resolution to generate global PSDs with a wider range of sizes than the ones obtained from any single resolution. Papadopoulos et al. (2009) tested this concept by adding pore-size classes quantified from 2D images obtained with a CT scanner at relatively low resolution and by imaging at higher resolutions resin impregnated soil blocks and thin sections; thus allowing the characterization of a wide range of pore sizes. Although they did not attempt to compare PSDs estimated with their method with independently measured ones, their approach should, in principle, result in more representative PSDs. A study using microCT images obtained at different resolutions would offer the advantage of using the same technique to image the soil across scales while extending the characterization of soil pores to 3D.

Consequently, the objective of this research was to evaluate the applicability of the geometrical and equivalent fluid filling approach proposed by Yang et al. (2009) using microCT images of four soils with contrasting properties, each imaged at four image resolutions. Global PSDs determined from the image analysis method were then compared with PSDs obtained using conventional water desorption and MIP techniques to independently check results obtained with the images.

MATERIAL AND METHODS

Soil Sample Preparation and Analysis

Four soils with contrasting soil properties (Table 1) were sampled from the EMBRAPA Southwest Cattle Center in São Carlos, Brazil, (Lat. 21°57′42″ S, Long. 47°50′28″ W, altitude 860 m). One undisturbed soil block (30 × 30 × 30 cm) was collected from the soil surface of each soil. The blocks were stored

in wooden boxes, transported to the laboratory and allowed to air-dry at room temperature for 30 d. Subsamples of the soil blocks were crushed and sieved through a 2-mm sieve for soil mechanical analysis with a g-ray attenuation system (Naime et al., 2001) and determination of soil particle density (ρ_p) with the pycnometer method (EMBRAPA, 1997). The amount of iron oxides (Fe_2O_3) was determined by selective dissolution extraction with sulfuric acid attack (EMBRAPA, 1997).

From the original soil block of each soil, cylindrical soil cores of approximately 4 cm in diameter by 2.5 cm in height, 2 cm × 2 cm and 1 cm × 2 cm were carved out using a sharp knife. Smaller soil samples of about 0.5 cm in diameter were taken as small round aggregates. In addition, one steel cylinder (5 cm diameter and 5 cm height) was sampled from soil blocks and used to estimate soil bulk density (ρ_b). Total porosity (ϕ_T) of the selected soils was estimated from ρ_b and ρ_p as: $\phi_T = 1 - \rho_b/\rho_p$.

MicroCT images were acquired with a cone beam benchtop X-ray microCT scanner from SkyScan, model 1172 (currently a Bruker manufactured system, Belgium). The X-ray tube operates at 100 kV and 100 mA, when using an aluminum/copper filter (0.5/0.04 mm thickness), positioned between the sample and the detector to block the soft X-rays and reduce beam-hardening artifacts and enhance image quality. The soil samples were stepwise rotated by 0.3° over 360° and 15 frames were acquired and averaged to represent the shadow projection of each rotational step. The samples were fixed onto the microCT scanner stage with double sided tape and modeling clay to avoid the movement of the samples during rotation. A modified Feldkamp cone-beam algorithm was used to reconstruct the two-dimensional cross-sectional images, with post alignment, smoothing, beam hardening, and ring artifact correction processes (Vaz et al., 2011). Cubic voxels with sizes of approximately 4, 6, 12, and 30 μm were obtained for sample diameters of 0.5, 1, 2, and 4 cm, respectively. The microCT images were binarized using a global, three-dimensional segmentation method (Kravchenko et al., 2009; Papadopoulos et al., 2009; Tarquis et al., 2009; Vaz et al., 2011). The software CTAn–Skyscan was used to obtain the average histogram based on analysis of linear attenuation coefficients of between approximately 950 (0.5; 1.0; and 2-cm diameter samples) and 450 (4-cm diameter samples) images (Fig. 2). The mean attenuation coefficient $\bar{\mu}$ used in the global segmentation method is given by:

$$\bar{\mu} = \frac{\mu_{air} + \mu_{particles}}{2} \quad [1]$$

where μ_{air} and $\mu_{particles}$ are the attenuation coefficients related to the air and particles, respectively. For this procedure, when the peak related to the air was not evident (see Fig. 2), the value adopted for μ_{air} was zero.

Table 1. Selected physical properties of the investigated soils.†

Soil type (symbol)	clay	silt	sand	Fe_2O_3	ρ_b	ρ_p	Textural class
		g g^{-1}		%	g cm^{-3}		
Typic Hapludox (S1)	0.292	0.074	0.634	5.2	1.43	2.70	sa cl lo
Rhodic Hapludox (S2)	0.732	0.147	0.121	4.5	1.38	2.75	cl
Rhodic Abaqualf (S3)	0.196	0.243	0.561	6.2	1.51	2.65	sa lo
Rhodic Kandiudalf (S4)	0.395	0.123	0.487	21.6	1.70	2.75	sa cl

†ρ_b, bulk density; ρ_p, particle density; sa, sandy; cl, clay; lo, loam.

Integration of Particle-Size Distributions Obtained with the Yang et al. (2009) Procedure

The procedure proposed by Yang et al. (2009) requires that the volume of interest (VOI) be completely contained in the soil sample, and that the number of slices (bi-dimensional images) included in the analysis be enough to identify and measure the largest pores in the axial direction. The latter condition is necessary because the process of finding the critical radius is interrupted when the regular object used to measure pore size finds a pore boundary (i.e., either the first or last slices of the VOI). Therefore, boundary artifacts arise if the VOI is smaller in the axial direction than the largest typical pore dimension (length or equivalent diameter). This is more significant for the smallest samples that are about 0.5 cm in diameter and have the highest image spatial resolution (voxel edge of 4 μm), where 100 slices represents only 0.4 mm in sample height, whereas for the largest soil sample (4 cm in diameter) the same number of slices represents 3 mm in sample height. Considering these two conditions, the investigated volumes were 4×10^8 voxels (1000 × 1000 pixels × 400 slices) for samples with diameter of 4, 2, and 1 cm and image pixel sizes of 30, 12, and 6 μm, respectively; and 2.56×10^8 voxels (800 × 800 pixels × 400 slices) for samples with diameters of 0.5 cm and 4 μm image pixel size.

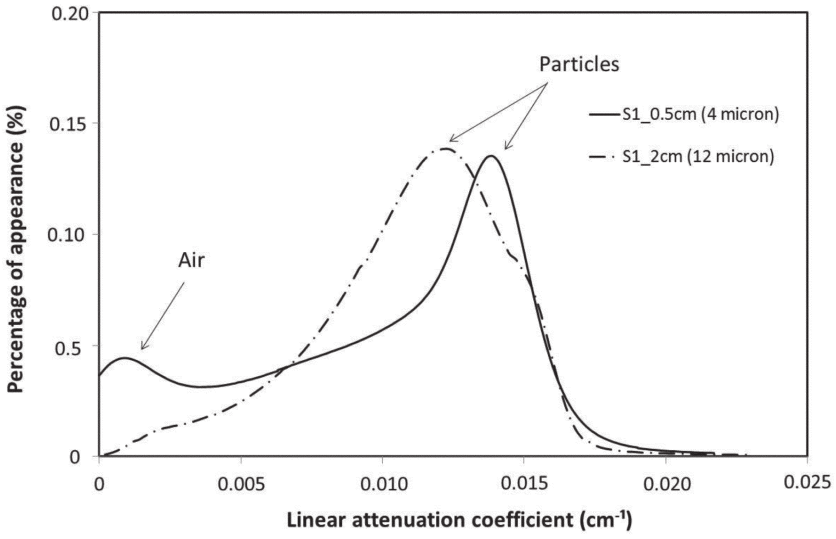

Figure 2. Attenuation coefficients for images of S1 soil at two resolutions (sample dimensions). Peaks related to air and particles are more evident at the resolution of 4 μm than at 12 μm.

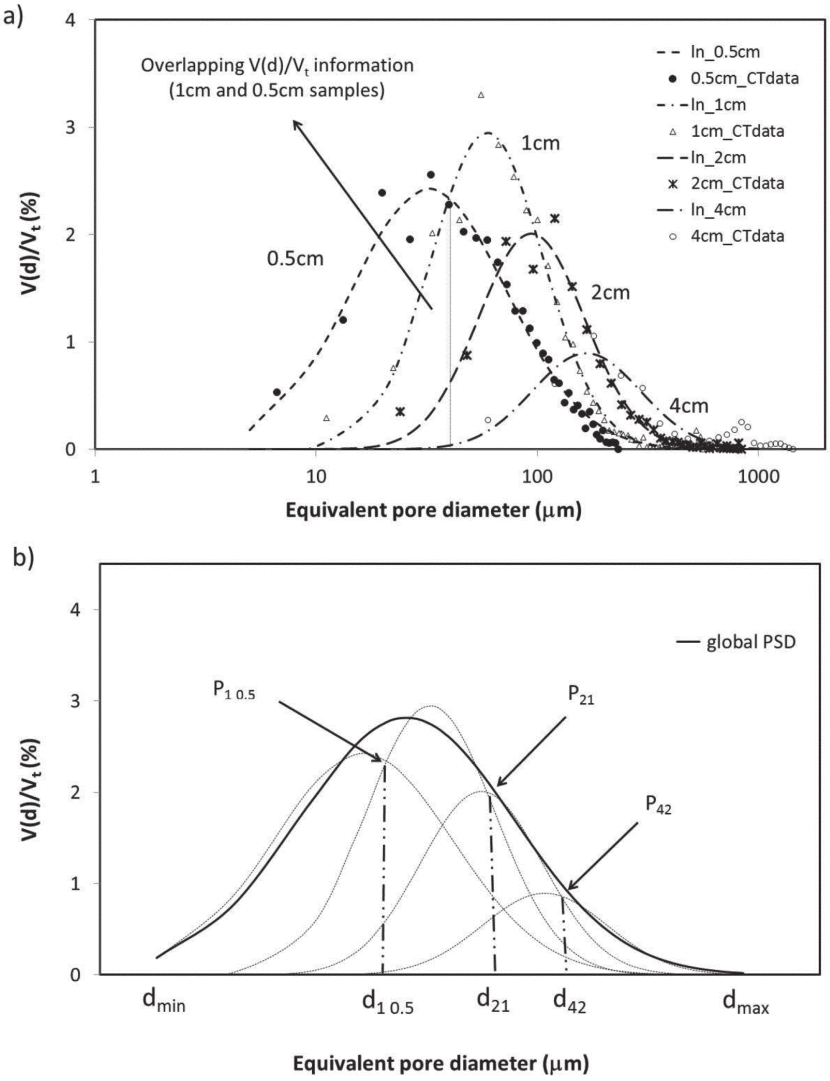

Figure 3. Schematic representation of the procedure applied to derive a global PSD of soil S1 from microCT images of four sample sizes with different image spatial resolutions. (a) overlapping information between 1- and 0.5-cm samples, and (b) points of intersection ($P_{10.5}$, P_{21}, and P_{42}); and their corresponding diameters (*d*min, *d*1 0.5, *d*21, *d*42, and d_{max}).

Pore-size distributions were obtained with using the MatLab program provided by Yang et al. (2009, supplemental material). The procedure can be summarized in the following steps: (i) determination of a critical radius r_c, for each pore unit identified in a binary image; r_c is defined as the maximum radius of an object of regular shape that is entirely encompassed in a pore (Fig. 1a); (ii) each voxel belonging to this defined pore region is counted and identified as the volume of the region whose critical radius is r_c; and (iii) subsequent incremental critical radii are found and assigned to their corresponding critical radius until the critical radius reaches the voxel unity (Fig. 1). The frequency distributions of pore diameters generated by this procedure were normalized to obtain relative pore volumes as $V_{rel} = V(d)/V_t$, where $V(d)$ is the measured volume for a given class of pore diameters and V_t is the total volume of the image or VOI.

In an attempt to derive more representative PSDs, we combined the PSDs determined from the microCT images of different sample sizes/image resolutions into a unique or global PSD curve for each soil. By virtue of their resolution and VOI physical extent, the four adjacent interpenetrating PSD curves covered somewhat different pore sizes, although there was also overlap between pore-size classes that were imaged at more than one resolution (Fig. 3a). It is a characteristic of the CT technique that higher resolutions are obtained with smaller samples. At the same time, relatively large and less numerous pores are not well represented in high resolution images. In principle, this makes PSDs from smaller samples better suited to represent V_{rel} information related to small pores, while the opposite is true for PSDs obtained at the lowest resolutions. Consequently, in the presence of overlapping PSDs, higher resolution data were selected to represent the smaller pore sizes in the overlapping range. The same guiding principle was used by Papadopoulos et al. (2009) to eliminate discrete pore-size classes imaged at two resolutions. The process of obtaining a single curve representing a set of PSDs obtained at different resolutions started by fitting each of the PSDs with a lognormal function using Origin software. The log–normal function was selected because it fitted the distributions reasonably well with r^2 values ranging from 0.81 to 0.98, but clearly other functions could be used. The crossover point(s) between fitted curves were used to truncate adjacent PSDs and discard the overlapping information. For example, in Fig. 3b, three intersection points were defined for each set of curves ($P_{10.5}$, P_{12}, and P_{42}), and the final PSD had information drawn from the 4- (d_{max} up to d_{42}), 2- (d_{42} to d_{21}), 1- (d_{21} to $d_{1\ 0.5}$), and 0.5-cm ($d_{1\ 0.5}$ to d_{min}) samples. Finally, the pore-size data representing the global PSD curve for a given soil was fitted with a lognormal function that integrated the selected data, (global PSD, Fig. 3b). The r^2 of the fits for the four soils varied between 0.95 and 0.97.

The area under the global PSD (Fig. 3b) represents the total accessed soil porosity and can be estimated with the following expression.

$$\phi_{accessed} = \sum_{d_1}^{d_n} \frac{V(d)}{V_t} = \frac{1}{V_t} \sum_{d_1}^{d_n} V(d) = \frac{\Delta V_{(d_n, d_1)}}{V_t} \quad [2]$$

where V_t is the VOI total volume, d is an equivalent measured pore diameter, and the summation is made from the largest (d_n) to the smallest (d_1) measured pore diameter to provide the total accessed soil porosity ($\phi_{accessed}$).

Soil Water Retention and Mercury Intrusion Porosimetry

After image acquisition with the microCT, the 4-cm diam. samples were saturated and water retention was determined according to Klute (1986) at water potentials of -0.1,−1, -2, -3, −4, −5, −6, −8, -10, -12 kPa (porous plate funnel) and -30 and -1500 kPa (pressure extractors). Since the MIP apparatus analyses small samples (maximum chamber size diameter is 1 cm), the 2-cm diameter scanned samples were shaped to approximately 1 cm cylindrical cores for analysis in a Poresizer 9320 (Micromeritics, USA), with applied pressures from 4 to 1500 kPa (equivalent soil pore diameters from approximately 320 to 0.8 μm) in 40 pressure increments. The SWRC data were fitted with the van Genuchten (1980) equation and the model was used to predict water contents retained at the pore sizes measured in the microCT images.

Mercury is a non-wetting liquid with a high value of surface tension and contact angle and needs pressure to be intruded in soils (van Brakel et al., 1981). According to the capillary or Washburn equation (Eq. [3]) the pressure P needed to intrude mercury into a cylindrical capillary of radius r is:

$$P=\frac{\left(2\sigma_{Hg}\ \cos\beta_{Hg}\right)}{r} \qquad [3]$$

where σ_{Hg} is the mercury surface tension and β_{Hg} is the contact angle between mercury and the capillary wall.

A SWRC can be derived from the PSD data obtained with the microCT image analysis, associating the measured pore radius (r) to the soil water potential (h) using the capillary rise equation [$h = (2\sigma\cos\beta)/r$; where σ is the water–air surface tension and β is the contact angle]. The smallest pixel size used in this study was 4 μm, which allows an image resolution or detectability of about 7 μm (Stock, 2008). According to the capillary raise equation, pores with a diameter of 7 μm can retain water up to a matric potential of about −40 kPa. Therefore, the microCT images analyzed by the Yang et al. (2009) algorithm produces PSD for equivalent pore diameters larger than about 7 μm and SWRC for equivalent matric potentials larger than about −40 kPa. The Root Mean Square Deviation (RMSD) between values of water contents estimated from measured SWRC, θ_i, and calculated from microCT images, $\hat{\theta}_i$, at the i*th* matric potential were quantified as:

$$\theta_{RMSD}=\sqrt{\frac{\sum_{i=1}^{n}\left(\hat{\theta}_i-\theta_i\right)^2}{n}} \qquad [4]$$

where n is the number of observations.

RESULTS AND DISCUSSION

Binarized microCT images of the four soils (S1 to S4) at four different sample sizes/image resolutions are presented in Fig. 4. Soils S1, S2 and S3 exhibit more round and elongated pores, while Soil S4 has more cracks and elongated pore structures. Small pores connecting larger ones are visible in all soils when image resolution increases. There is also a noticeable variability in the structure pattern of Soil S2, mainly because of the presence of relatively large and dense aggregates of about 5 mm in diameter, possibly because intra-aggregate pores in this heavy clay soil were below the detection limit.

As expected, accessed porosity increased with increasing image resolution because smaller pores were detected as image resolution increased (Fig. 5 and Table 2). At the highest resolution, the largest porosity value was measured in the image of Soil S1, which has the greatest content of sand particles. The lowest porosity was accessed in Soil S4 because of the relatively high amount of fine particles (clay and iron oxides), high bulk density and low total porosity of this soil (Table 1). The accessed porosities obtained with the global PSD approach were in general larger than the porosity accessed at the highest image resolution (Table 2). Using the proposed procedure, between 29% (Soil S4) to 74% (Soils S1 and S3) of the total porosity of each soil was accessed (Table 2). The remaining porosity ($\Delta\phi$ in Table 2) is not detected because it is composed of pores with diameters smaller

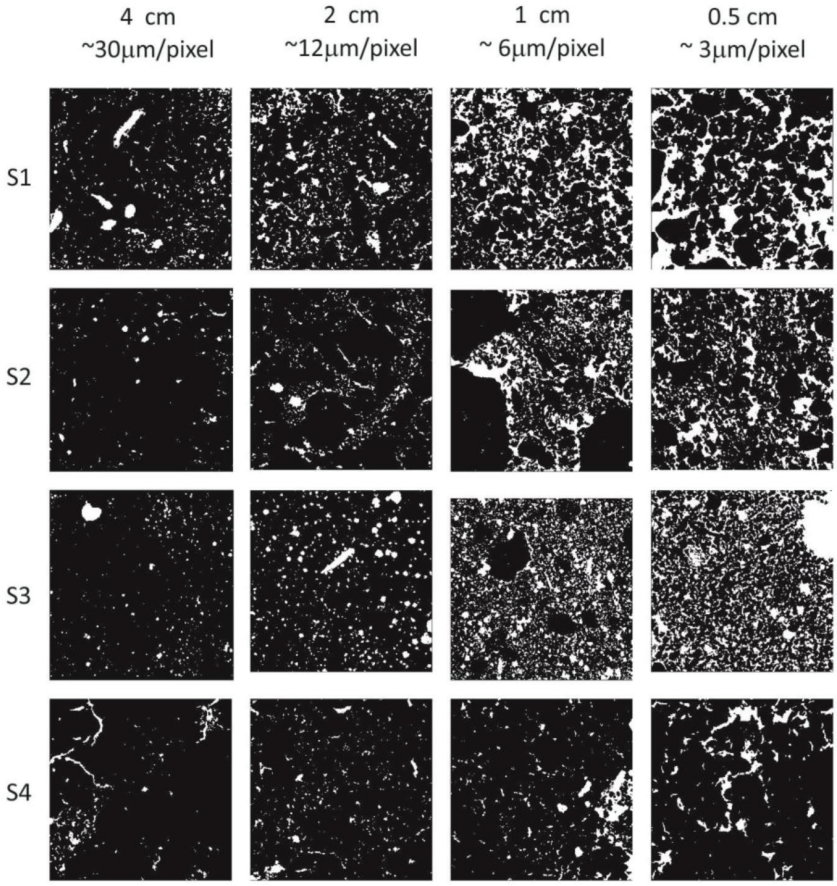

Figure 4. Binary microCT images of four soils (S1 to S4) at various sample/pixel sizes (white: pores; black: solid material).

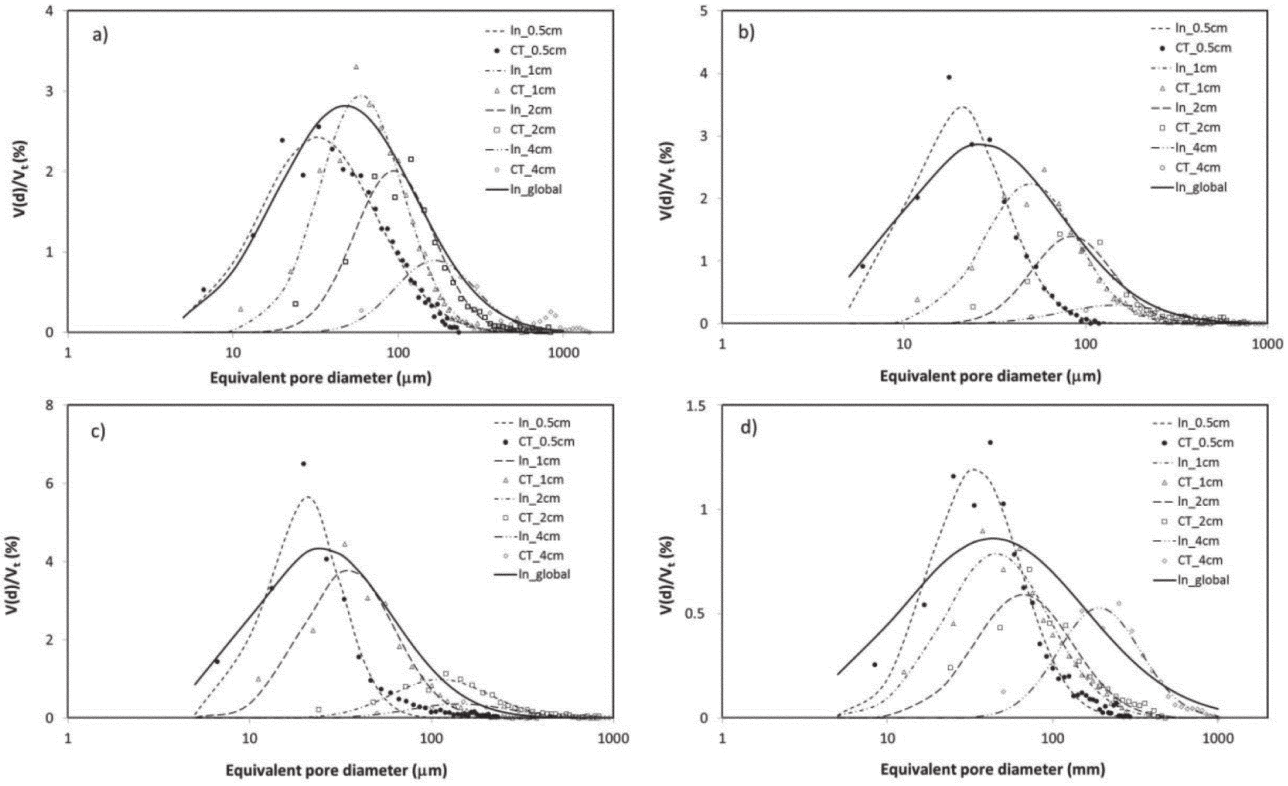

Figure 5. Pore-size distributions obtained with the Yang et al. (2009) approach applied to microCT images (400 slices) of four soils (a) S1; (b) S2; (c) S3; and (d) S4) each at sample sizes 0.5, 1.0, 2.0, and 4 cm and image spatial resolutions. Symbols are microCT-derived pore-size classes and lines are fits with a lognormal function. The thicker continuous line represents the lognormal fit of the global PSDs.

than about 7 μm, which is the limit of detectability with the image resolution used.

Differences in PSDs among soils were evaluated by segmenting the global PSD curves shown in Fig. 5 in six diameter classes, from 5 to 5000 μm (Table 3). Soil S1, with a sandy clay loam texture, had the largest accessed volume of pores for diameter classes larger than 50 μm, which agrees with the very high water permeability of this soil (Araújo et al., 2007). The largest volume of pores with diameters between 5 and 50 μm was measured in soil S3, probably due to the relatively high silt content of this soil when compared with the others soils (Table 1).

Table 2. Total accessed porosity obtained by pixel counting of the binarized microCT images for all soils (S1 to S4) at four different pixel sizes and with the global PSD (see Fig. 3). The porosity non-accessed ($\Delta\phi$) is estimated as the difference between total porosity, ϕ_T, and the porosity accessed in the global PSD.†

Pixel size (μm)	$\phi_{accessed}$ (cm^3 cm^{-3})			
	S1	S2	S3	S4
4	0.32	0.20	0.20	0.09
6	0.27	0.17	0.20	0.07
12	0.13	0.07	0.09	0.04
30	0.04	0.02	0.02	0.03
global PSD	0.34	0.27	0.27	0.10
ϕ_T	0.47	0.50	0.43	0.38
$\Delta\phi$	0.13	0.23	0.17	0.28

†$\Delta\phi$(porosity not accessed): ϕ_T - $\phi_{accessed}$ (global PSD).

The PSDs generated with the three techniques used in this study were in general in good agreement, particularly for soils S1 and S2 (Fig. 6). The PSDs obtained from the microCT images with the image-based method of Yang et al. (2009) and the procedure proposed in this study resulted in global PSDs that had intermediate values between the MIP and SWRC data for equivalent pore diameters larger than about 50 μm (all soils in Fig. 6). For equivalent pore diameters smaller than about 50 μm, the microCT-derived PSDs were similar to the SWRC data for Soils S1 and S2 and more related to the MIP data for Soils S3 and S4, although S3 had the most noticeable mismatch with the PSDs derived from SWRC and MIP. Since there was no general bias on the PSDs predicted from the microCT images and the measured ones, it is reasonable to conclude that the discrepancies

Table 3. Porosity ($\phi_{accessed}$) for each soil estimated from four microCT images combined into a global PSD (data from Fig. 5) separated by pore-size classes (Δd).

Δd	S1	S2	S3	S4
	$\phi_{accessed}$			
μm	%			
5–10	0.73	1.65	1.45	0.13
10–50	16.40	18.89	22.39	6.30
50–100	11.01	4.89	2.51	1.90
100–500	5.68	1.55	0.56	1.62
500–1000	0.18	0.01	0.01	0.06
1000–5000	0.01	0.00	0.05	0.00
TOTAL	34	27	27	10

among soils are probably caused by the properties of each soil pore system, such as pore connectivity and tortuosity, in relation to the operation principles of the MIP and SWRC techniques.

In general, PSDs obtained with the MIP technique had narrower peaks than the PSDs derived from SWRC. This is probably because SWRC works on desorption mode and equilibration is reached in days or weeks depending on the soil type, whereas the MIP technique operates on sorption or intrusion mode and typical duration time for each pressure step is in the order of a few seconds. For this reason, mercury intrusion is most likely to underestimate soil porosity especially for larger equivalent pore diameters (Giesche, 2006). On the other hand, measurements of water retention using desorption tend to overestimate the fraction of small pores in pore systems with relatively low pore connectivity, because regions or pockets of soil could become isolated from the drainage paths and, therefore, will not drain or will drain at a slower rate (Collis-George, 2012; Dal Ferro et al., 2015). This could be the reason for the larger fraction of pores smaller than 50 μm estimated by SWRC data in soils S3 and S4 (Fig. 6). Pore-size distributions of Soils S1 and S2 estimated from microCT images contained less pores > 50 μm than the corresponding PSDs estimated from water retention data (Fig. 6). This is opposite to what is typically found when comparing microCT and water retention derived PSDs (Rab et al., 2014; Dal Ferro et al., 2015) because the drainage of large pores is conditioned by their narrowest section or 'ink bottle' effect (Vogel and Roth, 1998; Hunt et al., 2013). A possible reason for the underestimation of the large pores in the microCT images in this study is that the lognormal fit integrating all individual PSDs did not properly represent the 'tails' of the distributions, therefore, excluding the larger pores. The threshold value used to binarize the images could certainly influence the amount and sizes of detected pores (Sezgin and Sankur, 2004; Taina et al., 2008; Houston et al., 2013). This is particularly true in those images where the attenuation coefficient for air was not evident (see Fig. 2). On the other hand, the use of images of several resolutions to build the PSDs most likely improved image sharpness for all pore sizes, making it easier to threshold the images (Houston et al., 2013). None of the factors that could potentially induce deviations between the estimated PSDs applied equally to all four soils, highlighting the problems of extracting PSDs using direct (3D images) or indirect (MIP and SWRC) methods and stressing the fact that the best techniques to process images may be soil-dependent.

The impact of PSDs estimated from microCT on water retention was assessed by converting pore sizes measured in 3D images to matric potentials using the capillary equation, and generating the cumulative distribution of water-filled pore volumes. To compare measured and estimated water retention curves, values of the non-accessed porosity, constituted by pore diameters below the detectability limit of 7 μm ($\Delta\phi$ in Table 2), were added to the accessed porosity as an offset for each soil. The best agreements between SWRC measured and estimated by image analysis were obtained for soils S2 and S4 (Fig. 7) as indicated by the lower RMSD values of these soils when compared with

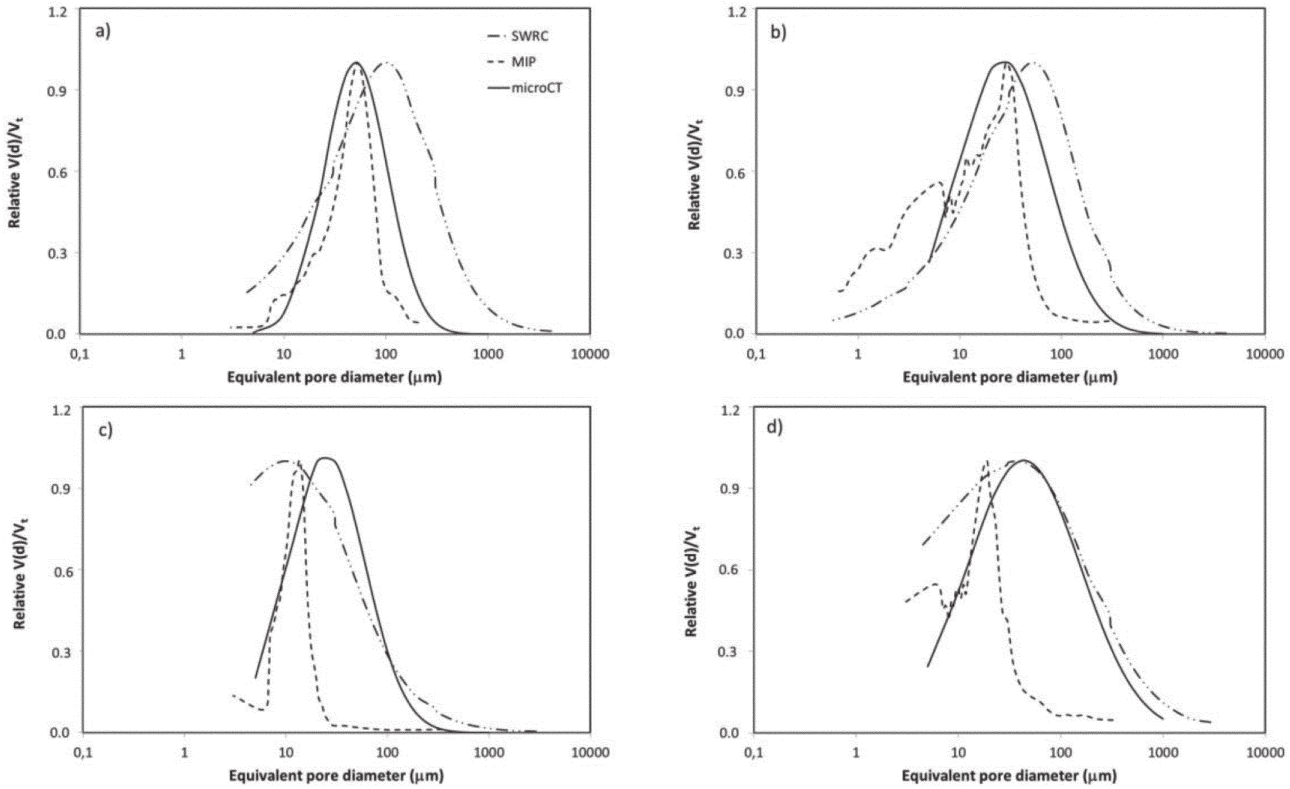

Figure 6. Global PSDs estimated from microCT images by integrating PSDs obtained at four resolutions (Fig. 5) compared with PSDs obtained from MIP and SWRC techniques for soils (a) S1, (b) S2, (c) S3, and (d) S4. Segmented lines were obtained by fitting the data with peak functions using Origin software.

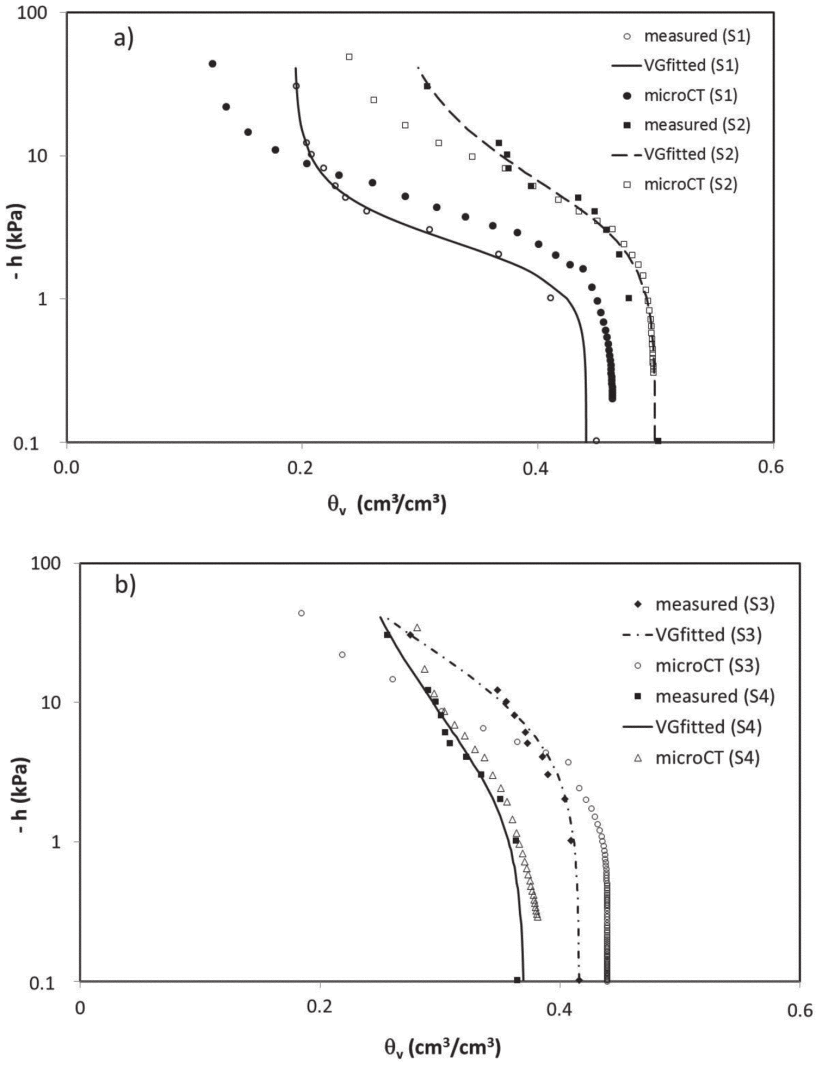

Figure 7. Soil water retention curves (SWRCs) estimated from microCT images (microCT), experimental SWRC (measured) and fitted with the van Genuchten (1980) equation (VGfitted) for soils (a) S1 and S2, and (b) S3 and S4.

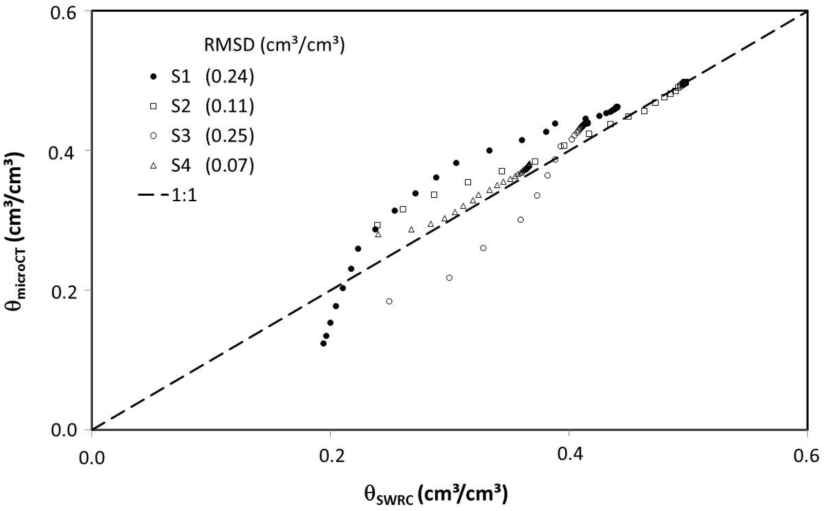

Figure 8. Correlation between measured volumetric soil water contents estimated from fits of the SWRCs shown in Fig. 7 (θ_{SWRC}) and the corresponding water contents estimated from microCT images ($\theta_{microCT}$). RMSD: root mean square deviation.

soils S1 and S3 (Fig. 8). Particle-size distributions estimated with the image analysis method proposed in this work predicted reasonably well the water retention curves at the wet range, but deviated from measured values at matric potentials between −6 and -10 kPa (Fig. 7). The failure of the image analysis technique to predict water retention at lower matric potentials is likely related to the absence of connectivity in the capillary bundle representation of the image-derived PSDs (Vogel and Roth, 1998). Soil water retention curves for Soils S1 and S3 estimated from image analysis did not correlate well with the experimental ones over the entire range of the measured curve (Fig. 8). The peculiarity of the predictions for these two soils is that the image-derived PSDs predicted greater water contents than measured ones for matric potentials larger than approximately −7 kPa, although the overall shape of the water retention function was reproduced reasonably well. The potential causes for this result are likely rooted in the technique used to derive the final PSD. Recently Tracy et al. (2015) took advantage of the possibility of identifying the water phase in CT images and imaged soil samples at equilibrium with different pressure potentials, thus providing a more direct estimation of water retained in soil. Extending their approach to different image resolutions would provide empirical evidence of the impact of connectivity in the estimation of water retention.

CONCLUSIONS

This work demonstrates the potential of combining information on pores sizes obtained at four resolutions ranging from 4 to 30 μm. Pore sizes obtained at different image resolutions were combined into a unique distribution for each soil (PSD). Predictions of water retention with the combined PSD resulted in water retention curves with shapes similar to the experimental ones in the range from saturation to matric potentials between −6 and −10 kPa, but predicted smaller than measured water contents for smaller matric potentials. This and other deviations observed in this work could have been caused by the simple capillary model used to predict water retention, but it could also be the result of image processing or the way the PSDs were estimated.

The procedure to combine and integrate PSDs from several resolutions is promising, but more research is needed to design tech-

niques to merge PSDs imaged at more than one resolution. The logical extension of this work is to develop models of pore systems that integrate information obtained at different resolutions and that include other pore metrics such as pore connectivity and tortuosity. Imaging of the water phase at equilibrium with a wide range of potentials would help refine such pore metrics.

ACKNOWLEDGMENTS

The authors gratefully acknowledge support from the Brazilian Agricultural Research Corporation (EMBRAPA), the Brazilian National Council for Scientific and Technological Development (CNPq) under grants no. 151679/2010, 304951/2013-7, and the Brazilian Innovation Agency (FINEP) under grant no. 01.06.0555.00. Daniel Gimenez acknowledges support from the National Institute of Food and Agriculture, U.S. Department of Agriculture, Hatch project 1008886 through the New Jersey Agricultural Experiment Station, Hatch project NJ07235.

REFERENCES

Araújo, R., W.J. Goedert, and M.P.C. Lacerda. 2007. Qualidade de um solo sob diferentes usos e sob cerrado nativo. (In Porteguese.) Rev. Bras. Cienc. Solo 31:1099–1108. doi:10.1590/S0100-06832007000500025

Cássaro, F.A.M., A.K. Borkowski, L.F. Pires, J.A. Rosa, and S.C. Saab. 2011. Characterization of a Brazilian clayey soil submitted to conventional and no-tillage management practices using pore size distribution analysis. Soil Tillage Res. 111:175–179. doi:10.1016/j.still.2010.10.004

Císlerová, M., and J. Votrubová. 2002. CT derived porosity distribution and flow domains. J. Hydrol. 267:186–200. doi:10.1016/S0022-1694(02)00149-X

Cnudde, V., and M.N. Boone. 2013. High-resolution X-ray computed tomography in geosciences: A review of the current technology and applications. Earth Sci. Rev. 123:1–17. doi:10.1016/j.earscirev.2013.04.003

Collis-George, N. 2012. A re-interpretation of the drainage moisture characteristic. Geoderma 189:87–90. doi:10.1016/j.geoderma.2012.05.008

Dal Ferro, N., P. Delmas, C. Duwing, G. Simonetti, and F. Morari. 2012. Coupling X-ray microtomography and mercury intrusion porosimetry to quantify aggregate structures of a cambisol under different fertilization treatments. Soil Tillage Res. 119:13–21. doi:10.1016/j.still.2011.12.001

Dal Ferro, N., P. Charrier, and F. Morari. 2013. Dual-scale micro-CT assessment of soil structure in a long-term fertilization experiment. Geoderma 204–205:84–93. doi:10.1016/j.geoderma.2013.04.012

Dal Ferro, N.A.G., C. Strozzi, P. Duwig, P. Delmas, F. Charrier, and F. Morari. 2015. Application of smoothed particle hydrodynamics (SPH) and pore morphologic model to predict saturated water conductivity from X-ray CT imaging in a silty loam Cambisol. Geoderma 255:27–34. doi:10.1016/j.geoderma.2015.04.019

EMBRAPA. 1997. Manual of soil analysis methods. (In Portuguese.) Embrapa-SNLCS, Rio de Janeiro, Brazil.

Flint, L.E., and A.L. Flint. 2002. Porosity. In: J.H. Dane and G.C. Topp, editors, Methods of soil analysis. Part 4. SSSA Book Series 5. SSSA, Madison, WI. p. 241-254.

Giesche, H. 2006. Mercury porosimetry: A general (practical) overview. Part. Part. Syst. Charact. 23:9–19. doi:10.1002/ppsc.200601009

Helliwell, J.R., C.J. Sturrock, K.M. Grayling, S.R. Tracy, R.J. Flavel, I.M. Young, W.R. Whalley, and S.J. Mooney. 2013. Applications of X-ray computed tomography for examining biophysical interactions and structural development in soil systems: A review. Eur. J. Soil Sci. 64:279–297. doi:10.1111/ejss.12028

Houston, A.N., S. Schmidt, A.M. Tarquis, W. Otten, P.C. Baveye, and S.M. Hapca. 2013. Effect of scanning and image reconstruction settings in X-ray computed microtomography on quality and segmentation of 3D soil images. Geoderma 207:154–165. doi:10.1016/j.geoderma.2013.05.017

Hunt, A.G., R.P. Ewing, and R. Horton. 2013. What's wrong with soil physics? Soil Sci. Soc. Am. J. 77:1877–1887. doi:10.2136/sssaj2013.01.0020

Jassogne, L., A. McNeill, and D. Chittleborough. 2007. 3D-visualization and analysis of macro-and meso-porosity of the upper horizons of a sodic, texture-contrast soil. Eur. J. Soil Sci. 58:589–598. doi:10.1111/j.1365-2389.2006.00849.x

Klute, A. 1986. Water retention: Laboratory methods. In: A. Klute, editor, Method of soil analysis. Part 1. SSSA Book Series 5. SSSA, Madison, WI. p. 635-662.

Kravchenko, A.N., M.A. Martin, A.J.M. Smucker, and M.L. Rivers. 2009. Limitations in determining multifractal spectra from pore-solid soil aggregate images. Vadose Zone J. 8:220–226. doi:10.2136/vzj2008.0008

Ma, R., C. Cai, Z. Li, J. Wang, T. Xiao, G. Peng, and W. Yang. 2015. Evaluation of soil aggregate microstructure and stability under wetting and drying cycles in two Ultisols using synchrotron-based X-ray micro-computed tomography. Soil Tillage Res. 149:1–11. doi:10.1016/j.still.2014.12.016

Mishra, B.K., and M.M. Sharma. 1988. Measurement of pore size distributions from capillary pressure curves. AIChE J. 34:684–687. doi:10.1002/aic.690340420

Naime, J.M., C.M.P. Vaz, and A. Macedo. 2001. Automated soil particle size analyzer based on gamma-ray attenuation. Comput. Electron. Agric. 31:295–304. doi:10.1016/S0168-1699(00)00188-5

Papadopoulos, A., A.P. Whitmore, R.P. White, S.J. Mooney, and N.R.A. Bird. 2009. Combining spatial resolutions in the multiscale analysis of soil pore-size distributions. Vadose Zone J. 8:227–232. doi:10.2136/vzj2008.0042

Peth, S., R. Horn, F. Beckmann, T. Donath, J. Fischer, and A.J.M. Smucker. 2008. Three dimensional quantification of intra aggregate pore space features using synchrotron radiation based microtomography. Soil Sci. Soc. Am. J. 72:897–907. doi:10.2136/sssaj2007.0130

Pierret, A., Y. Capowiez, L. Belzunces, and C.J. Moran. 2002. 3D reconstruction and quantification of macropores using X-ray computed tomography and image analysis. Geoderma 106:247–271. doi:10.1016/S0016-7061(01)00127-6

Rab, M.A., R.E. Haling, S.R. Aarons, M. Hannah, I.M. Young, and D. Gibson. 2014. Evaluation of X-ray computed tomography for quantifying macroporosity of loamy pasture soils. Geoderma 213:460–470. doi:10.1016/j.geoderma.2013.08.037

Stock, S.R. 2008. Recent advances in X-ray microtomography applied to materials. Int. Mater. Rev. 53:129–181. doi:10.1179/174328008X277803

Sezgin, M., and B. Sankur. 2004. Survey over image thresholding techniques and quantitative performance evaluation. J. Electron. Imaging 13:146–165. doi:10.1117/1.1631315

Taina, I.A., R.J. Heck, and T.R. Elliot. 2008. Application of X-ray computed tomography to soil science: A literature review. Can. J. Soil Sci. 88:1–19. doi:10.4141/CJSS06027

Taina, I.A., R.J. Heck, T.R. Elliot, and N. Scaiff. 2010. Micromorphological and X-ray mu CT study of Orthic Humic Gleysols under different management conditions. Geoderma 158:110–119. doi:10.1016/j.geoderma.2010.02.009

Tarquis, A.M., R.J. Heck, D. Andina, A. Alvarez, and J.M. Anton. 2009. Pore network complexity and thresholding of 3D soil images. Ecol. Complex. 6:230–239. doi:10.1016/j.ecocom.2009.05.010

Tracy, S.R., K.R. Daly, C.J. Sturrock, N.M.J. Crout, S.J. Mooney, and T. Roose. 2015. Three-dimensional quantification of soil hydraulic properties using X-ray Computed Tomography and image-based modeling. Water Resour. Res. 51:1006–1022. doi:10.1002/2014WR016020

van Brakel, J., S. Modry, and M. Svata. 1981. Mercury porosimetry: State of the art. Powder Technol. 29:1–12. doi:10.1016/0032-5910(81)85001-2

van Genuchten, M.T. 1980. A closed form equation for predicting the hydraulic conductivity of unsaturated soils. Soil Sci. Soc. Am. J. 44:892–898. doi:10.2136/sssaj1980.03615995004400050002x

Vaz, C.M.P., I.C. de Maria, P.O. Lasso, and M. Tuller. 2011. Evaluation of an advanced benchtop micro-Computed tomography system for quantifying porosities and pore-size distributions of two Brazilian oxisols. Soil Sci. Soc. Am. J. 75:832–841. doi:10.2136/sssaj2010.0245

Vogel, H.J., and K. Roth. 1998. A new approach for determining effective soil hydraulic functions. Eur. J. Soil Sci. 49:547–556. doi:10.1046/j.1365-2389.1998.4940547.x

Wang, W., A.N. Kravchenko, A.J.M. Smucker, W. Liang, and M.L. Rivers. 2012. Intra-aggregate Pore Characteristics: X-ray Computed Microtomography Analysis. Soil Sci. Soc. Am. J. 76:1159–1171. doi:10.2136/sssaj2011.0281

Wildenschild, D., and A.P. Sheppard. 2013. X-ray imaging and analysis techniques for quantifying pore-scale structure and processes in subsurface porous medium systems. Adv. Water Resour. 51:217–246. doi:10.1016/j.advwatres.2012.07.018

Yang, Z., X.F. Peng, D.J. Leen, and M.Y. Chen. 2009. An image-based method for obtaining pore-size distribution of porous media. Environ. Sci. Technol. 43:3248–3253. doi:10.1021/es900097e

Zhang, L.M., and X. Li. 2010. Microporosity structure of coarse granular soils. J. Geotech. Geoenviron. Eng. 136:1425–1436. doi:10.1061/(ASCE)GT.1943-5606.0000348